Biophysical Journal, Volume *111*

Supplemental Information

Rheology of the Active Cell Cortex in Mitosis

Elisabeth Fischer-Friedrich, Yusuke Toyoda, Cedric J. Cattin, Daniel J. Müller, Anthony A. Hyman, and Frank Jülicher

Supporting Material

Rheology of the active cell cortex in mitosis

E. Fischer-Friedrich,[1,2] Y. Toyoda,[1,3] C. J. Cattin,[4] D. J. Müller,[4] A. A. Hyman,[1] and F. Jülicher[2]

[1] *Max Planck Institute of Molecular Cell Biology and Genetics, Dresden, Germany*

[2] *Max Planck Institute for the Physics of Complex Systems, Dresden, Germany*

[3] *Institute of Life Science, Kurume University, Kurume, Japan*

[4] *Departement of Biosystems Science and Engineering, Eidgenössische Technische Hochschule Zürich, Basel, Switzerland*

I. ELASTIC MODULI OF A SIMPLE RHEOLOGICAL MODEL

In the following, we will derive the functional shape of the relaxation modulus and the complex elastic modulus for our simple rheological model introduced in the main text (Section "Rheology of the active cell cortex in mitosis"). This model relies on the assumption of a constant relaxation spectrum $h(\tau)$ up to a cut-off time scale τ_{max} after which the spectrum drops to zero (Fig. S1a). This simple form of the relaxation spectrum was derived as a simplified version of a reconstructed relaxation spectrum using measured rheological data (Fig. S1b) [1]. We define

$$h(\tau) = \begin{cases} K_h, & t < \tau_{max} \\ 0, & t \geq \tau_{max} \end{cases} \quad . \tag{S1}$$

Here, K_h is a stiffness that characterizes the spectrum amplitude and τ denotes the relaxation time variable. The relaxation modulus of a material with relaxation spectrum $h(\tau)$ is defined by the relation [2]

$$G(t) = \int_0^\infty h(\tau)\frac{\exp(-t/\tau)}{\tau}d\tau = \int_{-\infty}^\infty h(\tau)\exp(-t/\tau)\,d\ln(\tau) \quad , \tag{S2}$$

and the corresponding complex elastic modulus $G^*(\omega) = G'(\omega) + iG''(\omega)$ is given by

$$\begin{aligned} G'(\omega) &= \int_0^\infty \frac{\omega^2\tau}{(1+\omega^2\tau^2)}h(\tau)d\tau \\ G''(\omega) &= \int_0^\infty \frac{\omega}{(1+\omega^2\tau^2)}h(\tau)d\tau \quad . \end{aligned} \tag{S3}$$

Using Eq. (S2), a constant cut-off relaxation spectrum defined by Eq. (S1) gives rise to a relaxation modulus

$$G(t) = -K_h\mathrm{Ei}(-t/\tau_{\max}) \quad , \tag{S4}$$

where Ei denotes the exponential integral. Inserting the relaxation spectrum (S1) into Eqn. (S3), we find a storage and a loss modulus of the form

$$G'(\omega) = \frac{K_h}{2}\log(1+(\tau_{max}\omega)^2) \tag{S5}$$

$$G''(\omega) = K_h\arctan(\tau_{max}\omega) \quad . \tag{S6}$$

It is noteworthy that the storage modulus scales proportional to $\log(\omega)$ for large values of ω.

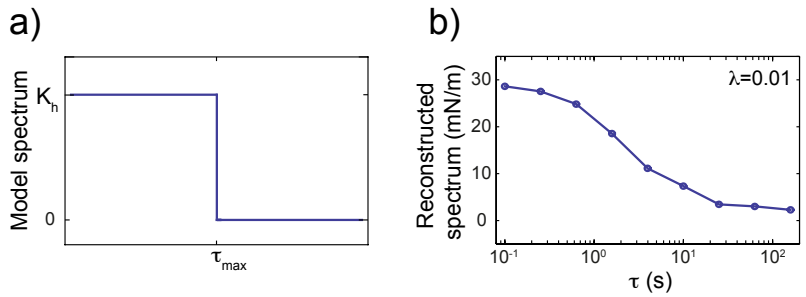

FIG. S1: Relaxation spectra of viscoelastic behavior. a) Relaxation spectrum of our rheological model. b) Relaxation spectrum reconstructed from rheological data presented in the main text (Section "Oscillatory forcing of the cell cortex"). The spectrum was calculated using Tikhonov regularization with regularization parameter $\lambda = 0.01$ [1].

For comparison, we will briefly discuss the functional shape of the relaxation spectrum $h(\tau)$, the relaxation modulus $G(t)$, and storage and loss modulus for the well-known Maxwell model and for a power law model. The Maxwell model exhibits a relaxation spectrum which is a delta peak $h(\tau) = k\delta(\tau - \tau_0)$. The associated relaxation modulus is the exponential decay $k\exp(-t/\tau_0)$ and storage and loss moduli can be calculated to be $k\omega^2\tau_0^2/(1+\omega^2\tau_0^2)$ and $k\omega\tau_0/(1+\omega^2\tau_0^2)$, respectively [2]. In the case of a power law rheology, the relaxation spectrum and the relaxation modulus are both a power law decay $\propto \tau^{-\beta}$, while storage and loss modulus are both proportional to ω^β [3].

II. DATA ANALYSIS OF STEPWISE UNIAXIAL CELL COMPRESSION

In the main text, we present experiments where cells in mitotic arrest were stepwise uniaxially compressed starting from different reference cell geometries at increasingly decreased cell heights. Each compression step was realized by a lowering of the cantilever by a distance Δh and accompanied by a force increase ΔF. In Fig. 3b, main text, and Fig. S11, we show the dependence of the force increase ΔF on normalized cell height reduction ξ in the reference state. To generate data depicted in Fig. 3b and Fig. S11, values of $\Delta F, \Delta h$ and normalized cell height reduction ξ were extracted for each compression step of a cell. In Fig. S11, values of $\Delta F/\Delta h$ were then plotted versus ξ. In Fig. 3b, data were normalized according to their estimated y-intercept and depicted in a log-linear plot.

Determination of $\Delta F, \Delta h$ and ξ. To probe cell stiffness at equal time scales, we extracted the force increase after a fixed compression time of 1 s (Note that the time span of the full compression step was partly longer ranging from $\approx 1-2$ s.). As we used a compression speed of 0.5 μm/s, a compression time of 1 s corresponds to a displacement of the AFM piezo by 0.5 μm. We will denote the cantilever height and the measured force after 1 s of compression by h_{1s} and F_{1s}, respectively. The height decrement Δh is calculated as $(h_{bef} - h_{1s})$, where h_{bef} denotes the cantilever height in steady state before the compression step. The value of Δh is generally smaller than the piezo deflection of 0.5 μm due to an increasing cantilever deflection. The corresponding force increase ΔF is estimated as $\Delta F = F_{1s} - F_{st,1s}$, where $F_{st,1s}$ is the steady state force corresponding to the cantilever height h_{1s}. This steady state force $F_{st,1s}$ was estimated as linear interpolation between steady state forces before ($F_{st,bef}$) and after ($F_{st,aft}$) the compression step. Therefore,

$$F_{st,1s} = F_{st,bef} + \frac{(h_{bef} - h_{1s})}{(h_{bef} - h_{aft})}(F_{st,aft} - F_{st,bef}) \quad ,$$

where h_{bef} and h_{aft} denote the cantilever height in steady state before and after the compression step, respectively. We experimentally verified that this is a very good approximation of steady state force for compression steps of $0.5-1\,\mu$m ($\lesssim 5\%$ error). To associate a value of ξ to a compression step, we calculated $\xi = 1 - 0.5(h_{bef})/(2R)$ which represents the cell height reduction before a compression step.

III. ANALOGY BETWEEN ELASTIC AND VISCOELASTIC DEFORMATIONS

In the main text, we were motivating the mechanical dominance of the cell cortex by comparing our experimental measurements of cell compression with theoretical calculations of uniaxial compres-

sion of elastic model cells (Fig. 3, main text). To motivate why the insight obtained from elastic deformations (Fig. 2, main text) applies to a viscoelastic object like a cell, we infer an analogy between the elastic and viscoelastic case. If a constant strain rate $\Delta\epsilon/\Delta t$ is applied to a stress-free, viscoelastic object in the time interval $[0, \Delta t]$, the peak stress at the end of this interval equals $\langle G(t)\rangle_{\Delta t}\Delta\epsilon$, where $\langle G(t)\rangle_{\Delta t}$ denotes the time average of the relaxation modulus in the interval $[0, \Delta t]$. Hence, provided a constant strain rate and a fixed time interval Δt of strain application, there is a stress-strain relation for the peak stress $\sigma(\Delta t)$ analogous to Hook's law with effective elastic constant $\langle G(t)\rangle_{\Delta t}$. This relation provides a quantitative analogy to the elastic case. In more simple terms one may say that an effective elastic constant $\langle G(t)\rangle_{\Delta t}$ may be associated to the viscoelastic system if a fixed range of time scales $[0, \Delta t]$ is probed.

IV. OSCILLATORY CELL FORCING AND DETERMINATION OF THE TWO-DIMENSIONAL ELASTIC MODULUS

Implementation of sinusoidal AFM cantilever motion. To implement cantilever motions for oscillatory cell compressions, we first approximated the sin-function as a piecewise-linear function (Fig. S2). To do this, we used four linear segments in the interval $[0, \pi/2]$, whose end points were optimized in terms of a least squares fit to match the sin-function most closely. The piecewise-linear function was then extended to the interval $[0, 2\pi]$ according to the symmetries of the sin-function. Oscillatory cantilever motions were then realized through an accordant piecewise-linear function (frequency- and amplitude-adapted) in terms of cantilever height ramps which were programed in a force script in the JPK AFM software. This force script was then carried out in the "repeat infinitely" mode at the desired average cantilever height.

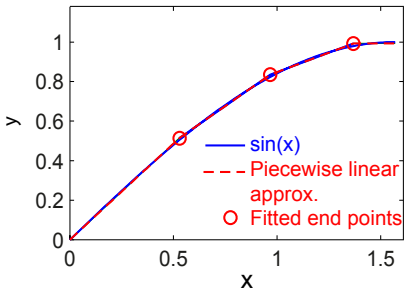

FIG. S2: Piecewise-linear approximation of sin function optimized by a least squares fit.

Cell height and cantilever oscillations are in phase. During oscillatory cell forcing, cantilever height oscillations alternate phases where the cantilever is pushed downwards with phases where the cantilever is lifted upwards. In phases of downwards movement, the cell height is forced to adapt immediately given a sufficiently stiff AFM cantilever. When the cantilever rises in the course of the oscillations, the cell follows the cantilever by increasing its height-extension since cellular surface tension drives it towards a round shape. This process of cell height relaxation may introduce a delay between cantilever height oscillations and cell height oscillations. We estimate the time scale of this delay as $\tau_{relax} \approx \frac{\eta_{cyt}}{p}\epsilon_{cyt}$ where η_{cyt} is the cytoplasmic viscosity, ϵ_{cyt} is a characteristic cytoplasmic bulk strain and p is the intracellular pressure excess. Intracellular cytoplasmic viscosity has been estimated in the range of $1 - 50\,\mathrm{Pa\,s}$ [4]. At a cantilever oscillation amplitude of $0.5\,\mu\mathrm{m}$ and an average cantilever height on the order of $10\,\mu\mathrm{m}$, a typical strain can be estimated as 0.05. Intracellular pressures measured are in the range of $100 - 500\,\mathrm{Pa}$ [5]. Therefore, the time scale τ_{relax} is expected to be $\leq 0.025\,\mathrm{s}$ which is an order of magnitude smaller than the smallest oscillation period sampled. We further checked whether measured phase shifts stay approximately constant if cantilever oscillation amplitudes (and thereby cytoplasmic strain and relaxation time) are reduced (Fig. S3). As this is indeed the case for the highest frequency measured ($f = 2\,\mathrm{Hz}$), we conclude that τ_{relax} is considerably smaller than $0.5\,\mathrm{s}$. We thus infer that cantilever height oscillations are to a good extent in phase with cellular height oscillations up to frequencies of $f = 2\,\mathrm{Hz}$.

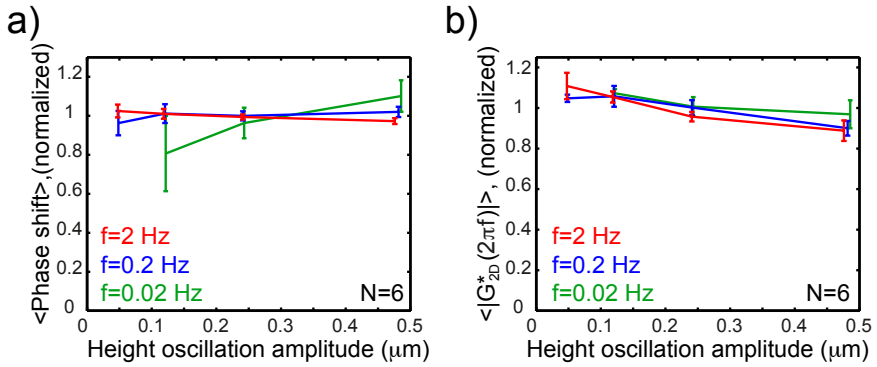

FIG. S3: Cell rheology in dependence of cantilever oscillation amplitude. a) Phase shift between stress and strain probed at cantilever oscillation amplitudes of 0.5 μm, 0.25 μm, 0.125 μm and 0.05 μm around a constant average cantilever height of $\approx$ 15 μm. At a given frequency, obtained phase shifts for different amplitudes were normalized by division through their mean value for each cell (N=6). Then the average of normalized amplitudes over six cells was calculated. For frequency $f = 0.02$ Hz, signal-to-noise ratios decreased (oscillations barely detectable) for declining oscillation amplitude giving rise to a large standard deviation and on average reduced phase shift. b) Same as in a but for magnitude of the estimated two-dimensional elastic modulus. Error bars show standard deviations. For $f = 0.02$ Hz, measurements at oscillation amplitudes of 0.125 μm and 0.05 μm gave too low signal-to-noise ratios and were therefore not considered.

Determining the two-dimensional complex elastic modulus. To determine the complex elastic modulus of cells from our measurements of oscillatory cell forcing, we determined a strain and an associated stress variable. As strain variable, we chose area strain of the total cell surface area. As associated stress variable, we calculated AFM force normalized to apparent tension $\gamma_{\mathrm{app}}(t)$. Defining stress and strain in that way, we could deduce a two-dimensional, complex elastic modulus from our oscillatory measurements defined as $G^*_{2D}(\omega) = \hat{\gamma}_{\mathrm{eff}}(\omega)/\hat{\epsilon}(\omega)e^{i\varphi(\omega)}$ where $\hat{\gamma}_{\mathrm{eff}}$ and $\hat{\epsilon}$ are estimated oscillation amplitudes of stress and strain, respectively, and φ is the phase shift between stress and strain.

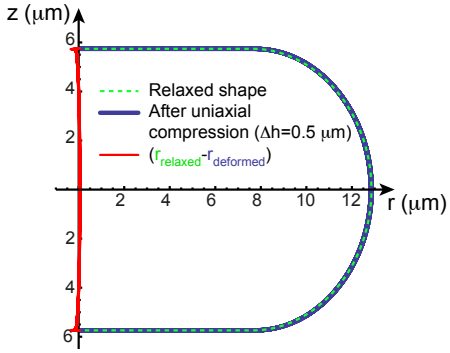

FIG. S4: Comparison of the steady state shapes of prestressed shells with and without elastic stresses due to uniaxial compression. Depicted are the profiles of the outer surface of an elastic shell in elastic equilibrium (dashed green) and of a shell with equilibrium height of 12 μm after a step of uniaxial compression by $\Delta h = 0.5\,\mu$m (dark blue). Shells have assigned an isotropic, in-plane prestress of 5000 Pa at a shell thickness of 200 nm and a total volume of 5000 μm^3. The shell height is set to 11.5 μm in both cases.

Data analysis of oscillatory measurements. In the following, we will describe how data from oscillatory cell compressions are analyzed in order to calculate stress and strain variables. For a cell measurement, we obtained the AFM cantilever height $h(t)$ and AFM force $F(t)$. From concurrent cell imaging, we could estimate a cellular volume V which was anticipated to stay constant during the measurement (Materials and Methods, main text). For every time point during the oscillation, cell surface area $A(t)$, cell curvature $H(t)$ and cell contact area with the compressing plates $A_{\mathrm{con}}(t)$ were estimated. To do this, we anticipated a shape of minimal surface area given the estimated cellular volume and the cantilever height $h(t)$ [5]. In steady state, we could show that this shape is a very good approximation of cell shape in mitosis due to present surface tension (deviations of less than 300 nm [5]). Calculations of the uniaxial compression of a (prestressed) elastic shell indicate that the shape after a compression step of $\Delta h = 0.5\,\mu$m is still very close to the shape of minimal surface area ($\leq 0.1\%$ deviation in surface area, Fig. S4). Using the assumption of a cell shape of minimal surface area, apparent tension $\gamma_{\mathrm{eff}}(t) = F(t)/(A_{\mathrm{con}}(t)2H(t))$ and surface area strain $\frac{A(t)}{\langle A\rangle}$ were calculated. Here, $\langle A\rangle$ denotes average surface area during oscillations.

We determined amplitudes and phase angles for calculated oscillatory signals of stress $\gamma_{\mathrm{eff}}(t)$ and strain $\frac{A(t)}{\langle A\rangle}$; for frequencies larger or equal to 1 Hz, typically ten and more oscillation periods were recorded and amplitudes and phase angles where estimated in terms of the discrete Fourier transform using Matlab. The discrete Fourier transform of the respective signal was estimated as a complex series $\{f_i\}_{i=1}^{N}$ by the command *fft*. We determined the peak of the absolute values of

$\{f_i\}_{i=1}^N$ at the index i_p. The phase angle is then calculated as the argument φ_{i_p} of the complex number $f_{i_p} = |f_{i_p}| \exp(i\varphi_{i_p})$ while the amplitude A of the signal is calculated as the integral over the peak

$$A = 2 \left(\sum_{i=\max(2,i_p-10)}^{i_p+10} |f_i|^2 \right)^{1/2} .$$

For frequencies smaller than 1 Hz, typically less than ten oscillation periods were recorded such that an analysis in terms of a Fourier transform was not reliable. Therefore, oscillation amplitudes and phase angles where estimated by performing a linear fit using the fit function $A\cos(2\pi t/T) + B\sin(2\pi t/T) + Ct$ where T is the oscillation period of the imposed cantilever oscillations. The phase angle of the signal was then calculated as $\arctan(A/B)$ while the amplitude was calculated as $A^2 + B^2$. As a control, we verified that for frequencies of around 1 Hz this method and the "Fourier method" give very close results for phase shift and signal amplitude. For oscillations periods of 50 and 100 s, typically only few oscillation periods were recorded, giving rise to a significant error of the extracted phase shift for associated frequencies.

V. DETERMINING RHEOLOGICAL PARAMETERS K_h AND τ_{max} FROM EXPERIMENTAL DATA

Fitting of storage and loss moduli. Our simple rheological model predicts a complex elastic modulus given by Eq. (S5) and (S6). This functional shape is fit to measured elastic moduli and allows thereby to determine K_h and τ_{max} from measured values of $G^*(\omega)$ for each cell. Experimental data of frequency-dependent storage and loss moduli were fit jointly by Eq. (S5) and (S6) with a least squares fit.

Fitting of force/tension decays. The relaxation modulus given by Eq. (S4) predicts stress relaxation after application of a compression step. Fitting of theoretically predicted stress decays to experimentally measured decays of apparent tension after steps of uniaxial cell compression allows to determine K_h and τ_{max} in an alternative way. Theoretically predicted tension decays $\gamma(t)$ were fit to the decay of measured apparent tension after a compression step of a cell. In the following, we describe how the fit function $\gamma(t)$ was calculated; measurements of compression steps were performed at a time resolution of $\Delta t = 0.1$ s. We calculated the tension generated in the time interval $[t_i, t_i + \Delta t]$ as

$$\gamma_{t_i \to t_i + \Delta t}(t) = \int_{t_i}^{t_i+\Delta t} G_{2D}(t - t')\dot{\epsilon}(t')dt' \approx \dot{\epsilon}(t_i) \int_{t_i}^{t_i+\Delta t} G_{2D}(t - t')dt'$$

using that the strain rate is roughly constant in the interval $[t_0, t_0 + \Delta t]$. The strain rate $\dot{\epsilon}(t)$ was estimated as area strain rate $(A_{cell}(t+\Delta t) - A_{cell}(t))/(A_{cell}(t_0)\Delta t)$, where $A_{cell}(t)$ is the estimated total cell surface area at time t. The overall tension at time t is then calculated as

$$\gamma(t) = \sum_{i=0}^{i=N} \gamma_{t_i \to (t_i + \Delta t)}(t)$$

where $\{t_i = t_0 + i\Delta t\}_{i=0}^{N}$ are time points of measurement during the process of cell compression. Fitted force decays as shown in Fig. 1c, main text, were generated by fitting the corresponding tension decay and then transforming fitted tension into force by the relation $F(t) = \gamma_{\text{eff}}(t)(A_{\text{con}}(t)2H(t))$, where $A_{\text{con}}(t)$ denotes the cell contact area with the compressing plates and $H(t)$ denotes the estimated mean curvature of the free cell surface.

VI. DEPENDENCE OF ELASTIC MODULI ON NORMALIZED CELL HEIGHT REDUCTION

We find that measured elastic moduli are to some extent dependent on the degree of cell height reduction (Fig. S5). The magnitude of elastic moduli tends to decrease for increasing values of normalized cell height reduction ξ for untreated cells. We speculate that geometrical effects may in part account for the decline of $|G^*_{2D}(\omega)|$ in dependence of ξ as suggested by calculations of the uniaxial compression of an elastic shell. At different levels of cell height reduction, shell bending at the contact line of shell and compressing plates gives different relative contributions to the overall compression force (Fig. S5c). For increasingly oblate shells, the relative contribution of bending goes down and the calculated stiffness value approaches the value of the elastic area bulk modulus of the shell ($K_A = Ed/2/(1-\nu)$) for strong cell height reduction. Here, E denotes the Young's modulus, d the thickness and ν the Poisson ratio of the shell.

Secondly, the decrease of $|G^*_{2D}(\omega)|$ for increasing ξ might partly originate from enhanced blebbing. The extrusion of small blebs, as commonly seen in cells with high surface tension at large values of ξ, might lead to an overestimation of cortical area strain in our analysis and therefore to an underestimation of elastic moduli at larger values of ξ. This effect may account for a decreased downwards slope of $|G^*_{2D}(\omega)|$ in the case of blebbistatin-treated cells.

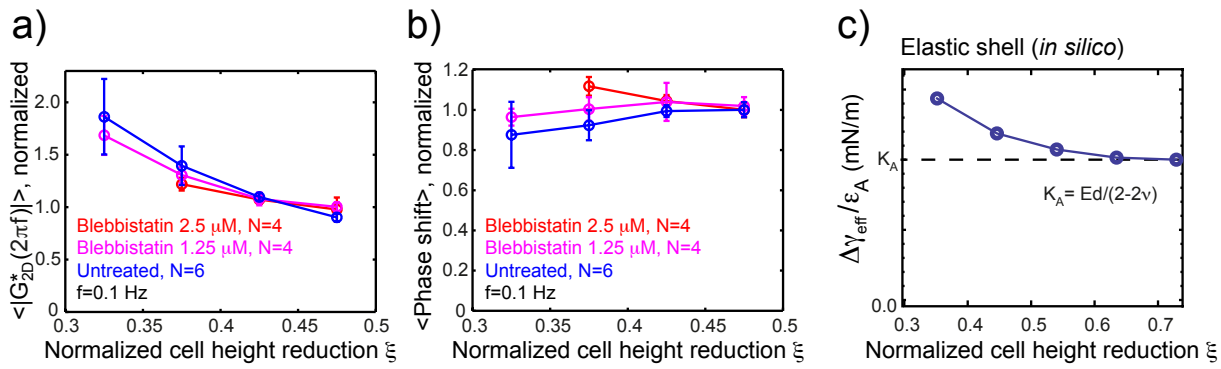

FIG. S5: Dependence of elastic moduli on the sampled degree of normalized cell height reduction. a) Magnitude of elastic modulus at $f = 0.1\,\mathrm{Hz}$ for untreated cells (blue, $N = 6$), cells treated with blebbistatin ($1.25\,\mu$M, magenta, $N = 4$ and $2.5\,\mu$M, red, $N = 4$). Each cell was sampled at different degrees of normalized cell height reduction at an oscillatory frequency of $0.1\,\mathrm{Hz}$ and an oscillation amplitude of $0.125\,\mu$m. Elastic moduli and phase shifts were calculated for each cell and normalized by division by their median value in the regime $\xi > 0.4$. Normalized data were then pooled and averaged over different cells. c) Stiffness values as obtained from finite element simulations of uniaxial compression of a prestressed, elastic shell (same parameters as in Fig. 2b, main text). Stiffness was calculated analogous to experimental measurements; the estimated increase of apparent tension $\Delta\gamma_{\mathrm{eff}}$ is divided by estimated area strain ϵ_A for the given deformation. For large ξ, stiffness converges to the value of the area bulk modulus $K_A = Ed/(2-2\nu)$, where d is the shell's thickness, and E and ν are the shell's Young's modulus and Poisson ratio, respectively ($E = 125\,\mathrm{kPa}$, $d = 200\,\mathrm{nm}$, $\nu = 0.49$).

VII. THE ACTIN CROSSLINKER α-ACTININ INFLUENCES TENSION AND ARCHITECTURE OF THE MITOTIC CORTEX

In mitotic cells, α-actinin-4 localizes strongly to the cell cortex (Fig. S6d). Knock-down of α-actinin-4 through RNA interference leads to a change of structural and mechanical properties of the mitotic cortex. In knock-down conditions, we find a reduction of cell surface tension (Fig. S6a,b) and a reduced fraction of cortical actin and myosin (Fig. S6c) as compared to control cells. In the course of mitosis, α-actinin-4 knock-down leads to a consistently reduced cell surface tension (Fig. S7). However, the duration of mitosis is not influenced by this tension drop (Fig. S7b).

Methods associated with Fig. S6 and S7: HeLa Kyoto cells expressing human H2B-GFP and mCherry-CAAX, human H2B-mCherry and human MYH9-GFP, human MYH9-GFP and Lifeact-mCherry or mouse ACTN4-GFP were cultured as described in the main text with additional $0.5\,\mu$g/ml Puromycin for cell lines with mCherry-tag (Life Technologies). RNA interference was performed as a forward transfection at a concentration of 10 nM with negative

controls (esiRNA: F-Luc, eupheria, HU-04832-1, siRNA: AllStars) and esiRNA or siRNA targeting ACTN4 (eupheria, HU-02773-1 or qiagen, Hs_ACTN4_5, SI02779973, target sequence: 5-acg cag cat cgt gga cta caa-3). Transfection was carried out using Lipofectamine RNAiMAX following the manufacturers instructions and assayed 48 hours post-transfection. For immunoblotting, primary antibodies were mouse monoclonal anti-ACTN4 (4D10, Sigma-Aldrich, USA) and rabbit monoclonal anti-GAPDH (14C10, Cell Signaling Technologies); secondary antibodies were HRP conjugated goat anti-rabbit (#170-6515, BioRad Laboratories, USA) and HRP conjugated goat anti-mouse (#170-6516, BioRad Laboratories). Cell surface tensions of cells in mitotic arrest were measured using the images acquired with an inverted light microscope (AxioObserver.Z1, Zeiss) and the cellular force response measured by a wedged cantilever mounted in the AFM head (CellHesion 200, JPK Instruments AG) (Fig. S7). Cells chemically arrested in prometaphase showing monopolar spindles were selected based on GFP fluorescence. The cantilever was lowered on the cell to a pre-set height and the resulting varying force was recorded over time. Once a steady plateau force value was reached, DIC and fluorescence images at the equatorial plane of the confined cell were recorded using a 20x air objective. All microscopy equipment was placed and experiments were carried out in a custom-made isolation box at 37°C (The Cube, Life Imaging Services, Switzerland). For experiments where cells were monitored during their passage through mitosis (Fig. S7), the experimental set-up consisted of an AFM (Cellhesion 200, JPK Instruments) mounted on an inverted confocal microscope (Observer.Z1, LSM 700, Zeiss). A 63x/1.3 LCI Plan-Neofluar water immersion objective (Zeiss) was used and images were recorded every 2 minutes. The cells were maintained at 37◦C using a Petri dish heater (JPK Instruments). AFM cantilevers used where modified to hold terminal wedges compensating for the intrinsic 10° tilt and produced as described before [6, 7].

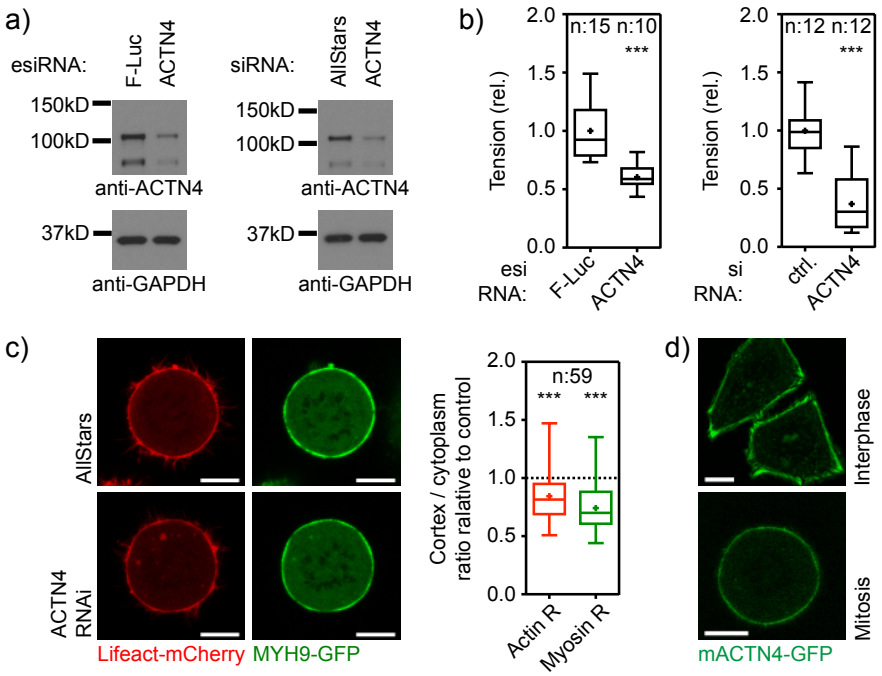

FIG. S6: RNAi-mediated depletion of α-actinin-4 results in decreased mitotic cell surface tension and altered cortical actin and myosin localization. a) Western blots of whole cell lysates of HeLa Kyoto cells expressing H2B-GFP and mCherry-CAAX, RNAi treated as indicated, using the antibodies indicated. b) Tension data of chemically arrested (2 μM S-Trityl-L-cysteine (STC)) mitotic HeLa Kyoto cells expressing H2B-GFP and mCherry-CAAX, RNAi treated with the constructs indicated, submitted to a height confinement assay. Values relative (rel.) to negative control average. ctrl., control cells c) Example images (left) and batch collected data (right) of chemically arrested (2 μM STC) mitotic HeLa Kyoto cells expressing MYH9-GFP and Lifeact-mCherry, RNAi treated with the constructs indicated, submitted to a height confinement assay. Values relative to negative control average. R, cortex/cytoplasm ratio of fluorescence intensity as detailed in Ramanathan *et al.* [8]. d) Example confocal micrograph of HeLa Kyoto cells expressing mACTN4-GFP with interphase- (top) and mitosis-specific (bottom) localization of mACTN4-GFP. Box, 25th to 75th percentile; Line, median; Whiskers, minimum to maximum; +, mean; n, number of cells characterized. Scale bar, 10 μm. Statistical significance was determined using the Mann-Whitney-test; ***, $p \leq 0.001$.

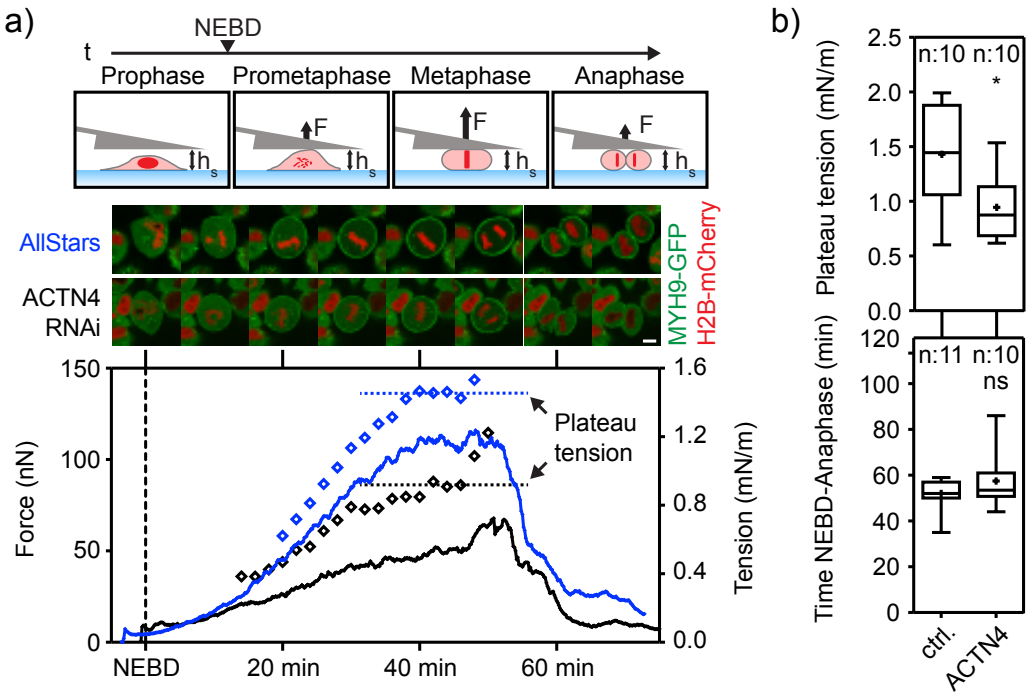

FIG. S7: RNAi-mediated depletion of α-actinin-4 results in decreased cell rounding tension trans-mitotically. a) Sketch (top), example force profiles (middle) and example confocal microscopy images (bottom) of HeLa Kyoto cells expressing H2B-mCherry and MYH9-GFP, RNAi treated with the constructs indicated, submitted to a trans-mitotic height confinement assay. Lines represent force traces and empty diamonds represent tension values. t, time; NEBD, nuclear envelope breakdown; F, force; h_s, set height. b) Plateau tension (top) and time from NEBD to anaphase onset (bottom) for cells analyzed as exemplified in a. Scale bar, 10 μm. Box, 25th to 75th percentile; Line, median; Whiskers, minimum to maximum; +, mean; n, number of cells characterized. Scale bar, 10 μm (all images). Statistical significance was determined using the Mann-Whitney-test; *, $p \leq 0.05$.

VIII. FINITE ELEMENT ELASTIC MODEL OF UNIAXIAL CELL COMPRESSION

Calculations were performed as finite element simulations in Comsol Multiphysics using the structural mechanics module. The program computed a stationary solution of an axisymmetric problem using linear elasticity theory. Before the deformation, the elastic model cell is set to be in its (elastic) equilibrium shape. Equilibrium shapes are chosen at different heights but identical cell volumes ($V = 5000\,\mu\mathrm{m}^3$).

The elastic model cell (shear-elastic bulk or shell) is sandwiched between two parallel, circular plates of high rigidity (E=200 GPa, ν =0.3) with a thickness of $1\,\mu$m. During a step of cell compression, both plates are moved towards each other by a defined distance $\Delta h/2$ (*prescribed displacement*). Contact between plates and model cell was defined through two *contact pairs* that included the upper (lower) boundary of the rectangle and the upper (lower) half of the model cell surface. By default, height decrements during cell compression were set to $\Delta h = 0.5\,\mu$m. Calculating height decrements Δh in between $0.1 - 1\,\mu$m yielded force increases scaling linearly with Δh.

Shear-elastic bulk. The first type of model cell was defined as an isotropic, elastic body. For simplicity, we defined its shape as a body of revolution generated by a rectangle and an adjacent semi-circle (black wire-frame in Fig. 2a, main text) with Young's modulus $E = 1000\,\mathrm{Pa}$ and Poisson ratio $\nu = 0.49$. The bulk volume was set to $5000\,\mu\mathrm{m}^3$. Mesh size was set as *user-controlled mesh* using the *general physics* option *finer*. The *free triangular* feature was used to refine the meshing associated to the bulk and the plate surface by setting the minimal element size to 0.05 μm. Again, with the *free triangular* option, the maximum element size in the bulk interior was set to 0.15 μm.

Elastic shell. The second type of model cell was defined as elastic shell of 200 nm thickness ($E = 125\,\mathrm{kPa}$ and Poisson ratio $\nu = 0.49$). The cell's shape was defined by the contour of a minimal surface area [5] with a total cell volume of $5000\,\mu\mathrm{m}^3$. The respective curve representing the free cell boundary is generated by Mathematica and then exported as a text file. This file is then imported into comsol as *interpolation curve*. The inner shell surface is defined from the outer surface subtracting the surface normal vector multiplied by the shell thickness. Furthermore, we assigned a uniform, constant mechanical prestress that mimics active tension in the cortex due to the presence of myosin motors. This is realized by assigning an *initial stress* to the shell domain by use of the structural mechanics module. The prestress is a constant, isotropic in-plane stress in the shell of magnitude σ_{act} (by default $5000\,\mathrm{Pa}$). In cylindrical coordinates (r, φ, z), the prestress

was assigned as

$$\begin{pmatrix} \sigma_{act} n_z^2 & 0 & -\sigma_{act} n_z n_r \\ 0 & \sigma_{act} & 0 \\ -\sigma_{act} n_z n_r & 0 & \sigma_{act} n_r^2 \end{pmatrix} \tag{S7}$$

where n_z and n_r are the component of the normal vector of the inner shell surface projected onto the z- and r-axis, respectively. For this definition of the stress, the normal vectors on the surface of the shell need to be referenced in the entire shell domain. To achieve this, we defined a *component coupling* operator of the type *general extrusion* with the source defined as inner shell boundary. At the inner boundary of the shell a *boundary load* in terms of a constant pressure is declared, that ensures conserved cell volume. The appropriate internal pressure was determined by repeatedly carrying out the simulation of uniaxial compression and determining resultant cell volume along with linear extrapolation of pressure values until a volume change of less than 0.02% was achieved. The shell mesh was defined as *user-controled mesh* using the *general physics* option *extra fine*. The *free triangular* feature was used to refine the meshing associated to the domain of the shell, the outer boundary of the shell and the surface of the disk-shaped plate that is in contact with the shell. The *maximum element size* inside the domain of the shell was set to 0.05 μm. The *maximum element size* of contacting plate surface was set to 0.1 μm. In addition, the *maximum element size* of the outer shell boundary was set to 0.05 or 0.025 μm, where the smaller value was used for shell heights of 6 and 8 μm, only.

In the case of the shell, ΔF as depicted in Fig. 3a,b, main text, is calculated as the force exerted on the plates after the compression step subtracted by the steady state force (due to prestress) at the new cell height.

IX. ALTERNATIVE ANALYSIS OF OSCILLATORY CELL FORCING

To compare our results with previous measurements that showed three-dimensional complex elastic moduli of cells, we also performed an alternative analysis of our data calculating effective three-dimensional Young's moduli. Using the most simple approach, we chose as stress variable $F(t)/\langle A_{eq}\rangle$ where $F(t)$ denotes time-dependent measured force, and $\langle A_{eq}\rangle$ denotes the average cross-sectional area at the cell equator. This geometrical parameter is directly obtained from cell imaging. We used $(\langle h\rangle - h(t))/\langle h\rangle$ as strain variable, where $h(t)$ denotes time-dependent cell height and $\langle h\rangle$ denotes its average. From this analysis, we obtain effective frequency-dependent cell elastic moduli in the range of $100 - 1500$ Pa for mitotic cells (Fig. S8a). For interphase cells, we

obtain values in the range $10 - 500$ Pa (Fig. S8b) which are comparable to effective cell elastic moduli reported earlier for rounded interphase cells [9, 10]. Note, that for this alternative analysis, storage and loss moduli derived from our model (Eqn. (4) and (5), main text) do not provide a good fit. A power law fit captures the calculated storage and loss moduli more closely. (We fitted $G'(\omega) = A\pi\omega^\beta \csc(\pi\beta/2)/2$ and $A\pi\omega^\beta \sec(\pi\beta/2)/2$ obtaining $A = 195\,\mathrm{Pa}$ ($68\,\mathrm{Pa}$) and $\beta = 0.2$ ($\beta = 0.24$) for mitotic cells (interphase cells).) However, in particular for mitotic cells (Fig. S8a), the loss modulus deviates from a power law behavior as it levels off at larger frequencies.

Interestingly, the effective 3D storage and loss moduli obtained in this alternative analysis look more similar to previously published data and show a different frequency dependence than the storage and loss moduli of the cortical layer discussed in Section 5, main text. The reason why the frequency dependence is different stems from the fact that the geometric factors used to define cortical 2D moduli are time-dependent. Time-dependent 2D cortical tension is defined as $\gamma_{\mathrm{eff}}(t) = F(t)/(A_{\mathrm{con}}(t)2H(t))$, where $A_{\mathrm{con}}(t)$ is the time-dependent contact area of the compressed cell and $H(t)$ is the mean curvature of the free cell surface. During oscillatory cell forcing, a periodic cell height change $h(t) = h_0 + \tilde{h}\exp(i\omega t)$ is imposed. Measured force and derived cortical tension oscillate accordingly as $F(t) = F_0 + \tilde{F}\exp(i\omega t)$ and $\gamma_{\mathrm{eff}}(t) = \gamma^0_{\mathrm{eff}} + \tilde{\gamma}_{\mathrm{eff}}\exp(i\omega t)$ and are in general phase-shifted with respect to cell height oscillations such that $\tilde{F}$ and $\tilde{\gamma}_{\mathrm{eff}}$ are complex numbers. To linear order, we have

$$F(t) = G_0\gamma^0_{\mathrm{eff}} + \left(\gamma^0_{\mathrm{eff}}\tilde{G} + G_0\tilde{\gamma}_{\mathrm{eff}}\right)\exp(i\omega t)\,,$$

where we have introduced a time-dependent geometric factor $G(t) = A_{\mathrm{con}}(t)2H(t)$ which oscillates periodically as $G(t) = G_0 + \tilde{G}\exp(i\omega t)$ in phase with height oscillations. Therefore,

$$\tilde{F} = \left(\gamma^0_{\mathrm{eff}}\tilde{G} + G_0\tilde{\gamma}_{\mathrm{eff}}\right).$$

Performing this analysis, we find that the real and imaginary part of $\tilde{F}$ and $\tilde{\gamma}_{\mathrm{eff}}$ are not proportional to each other due to the presence of the prestress γ^0_{eff}. Note that in passive systems, geometric changes usually enter to second order and therefore do not have such an effect. Thus the cell cortex with its actomyosin-induced active tension exhibits different rheological behavior when analyzed using the proper geometric factors as compared to a conventional interpretation where stress is essentially identified with force.

Finally, we also derived an effective, long-term 1D-stiffness of mitotic cells in Fig. S8c. This effective stiffness originates from a steady-state cell surface tension which mainly relies on active cortical tension in mitotic cells [5]. This stiffness was calculated from an increase of steady state force upon

stepwise cell height reduction (same data as in Fig. 3b, main text, each color codes for a single cell measured). Clearly, this effective stiffness increases for increasingly depressed cell heights. This trend is expected if measured steady state forces originate from a largely constant active cortical tension.

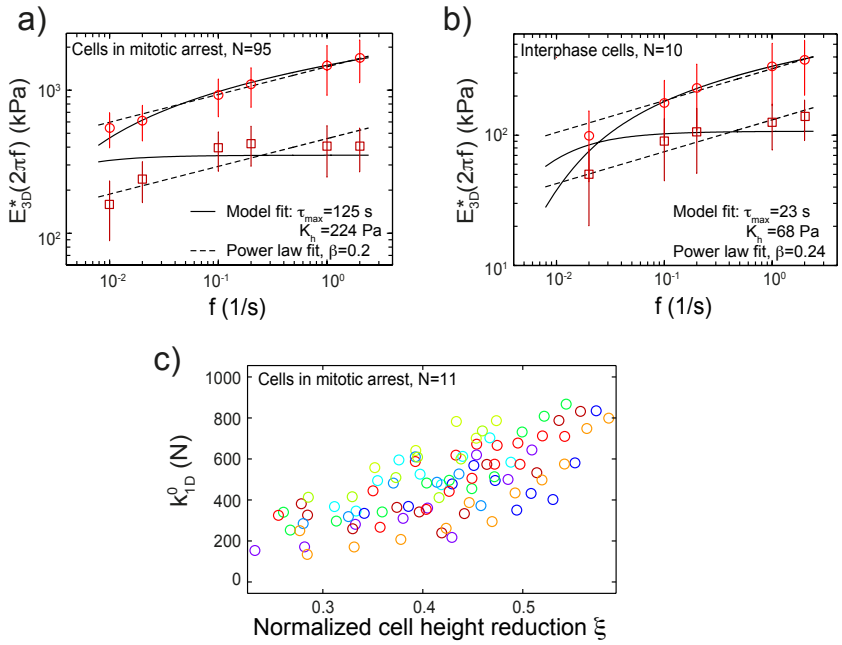

FIG. S8: Apparent dynamic Young's moduli of cells obtained from oscillatory cell forcing using a simple alternative data analysis. a) Effective dynamic Young's modulus of cells in mitotic arrest. b) Effective dynamic Young's modulus of cells in interphase. c) Effective 1D stiffness of mitotic cells derived from an increase of steady state force upon stepwise cell height reduction (same data as in Fig. 3b, main text, each color codes for a single cell measured). $k^0_{1D}(\xi) = \Delta F_{st}(\xi)/(\Delta h/2R)$ where $\Delta F_{st}(\xi)$ denotes the change in steady state force upon a compression step of Δh performed at a cell shape of normalized cell height reduction ξ. R denotes the cell radius associated to a spherical cell shape at constant cell volume.

[1] Honerkamp, P. J., and J. Weese, 1993. A nonlinear regularization method for the calculation of relaxation spectra. *Rheologica Acta* 32:65–73.

[2] Phan-Thien, N., 2012. Understanding Viscoelasticity: An Introduction to Rheology. Springer Science & Business Media.

[3] Kollmannsberger, P., and B. Fabry, 2011. Linear and Nonlinear Rheology of Living Cells. *Ann Rev Mater Res* 41:75–97.

[4] Wirtz, D., 2009. Particle-Tracking Microrheology of Living Cells: Principles and Applications. *Ann Rev Biophys* 38:301–326.

[5] Fischer-Friedrich, E., A. A. Hyman, F. Jülicher, D. J. Müller, and J. Helenius, 2014. Quantification of surface tension and internal pressure generated by single mitotic cells. *Sci Rep* 4:6213.

[6] Stewart, M. P., A. Hodel, A. Spielhofer, C. J. Cattin, D. J. Müller, and J. Helenius, 2013. Wedged AFM-cantilevers for parallel plate cell mechanics. *Methods* 59:186–194.

[7] Cattin, C. J., M. Düggelin, D. Martinez-Martin, C. Gerber, D. J. Müller, and M. P. Stewart, 2015. Mechanical control of mitotic progression in single animal cells. *PNAS* 112:11258–11263.

[8] Ramanathan, S. P., J. Helenius, M. P. Stewart, C. J. Cattin, A. A. Hyman, and D. J. Müller, 2015. Cdk1-dependent mitotic enrichment of cortical myosin II promotes cell rounding against confinement. *Nat Cell Biol* 17:148–159.

[9] Chan, C. J., A. E. Ekpenyong, S. Golfier, W. Li, K. J. Chalut, O. Otto, J. Elgeti, J. Guck, and F. Lautenschlger, 2015. Myosin II activity softens cells in suspension. *Biophys J* 108:1856–1869.

[10] Rosenbluth, M. J., W. A. Lam, and D. A. Fletcher, 2006. Force Microscopy of Nonadherent Cells: A Comparison of Leukemia Cell Deformability. *Biophys J* 90:2994–3003.

X. SUPPLEMENTARY FIGURES

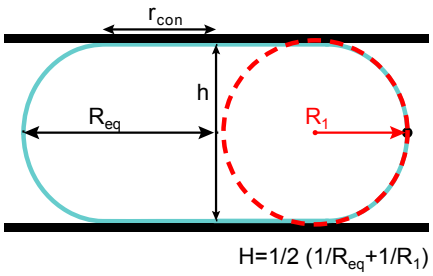

FIG. S9: Schematic of a cell confined between two parallel plates. During each measurement, the equatorial radius R_{eq} and the cell height h where measured. The mean curvature of the free cell surface area is calculated as $H = 0.5(1/R_1 + 1/R_{eq})$ using the two radii of principle curvatures in the equatorial plane. The principle curvature radius R_1 associated to the azimuthal direction is approximated as $R_1 \approx h/2$. Note that the mean curvature on the free cell surface is expected to be constant on the free cell surface due to Laplace's law [5]. The radius of contact r_{con} is the radius of the disk-shaped contact area with the plates.

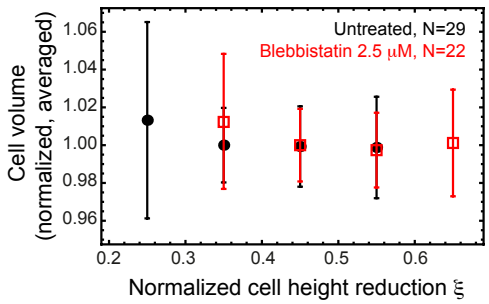

FIG. S10: Estimated cellular volume shows no trend of volume increase or decrease upon increasing uniaxial cellular compression (untreated: black, blebbistatin 2.5 μM: red). Cell volume was estimated for each level of height reduction using the cell's equatorial radius and assuming a shape of minimal surface area. Estimated volumes for one cell were normalized by division through its median volume. Error bars represent standard deviations.

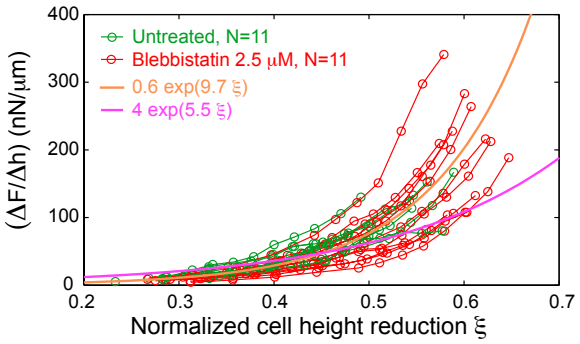

FIG. S11: Force increase after 1 s of uniaxial cell compression at constant speed. Connected data points correspond to the measurement of one cell at different degrees of cell height reduction ξ (untreated cells: green, N=11, blebbistatin-treated cells (2.5 μM): red, N=11). Orange and magenta lines indicate the trend of exponential functions with exponents of slope 5.5 and 9.7 which are expected for the scenario of a shear-elastic bulk or an elastic shell, respectively. Data are identical with those used in Fig. 3b, main text.

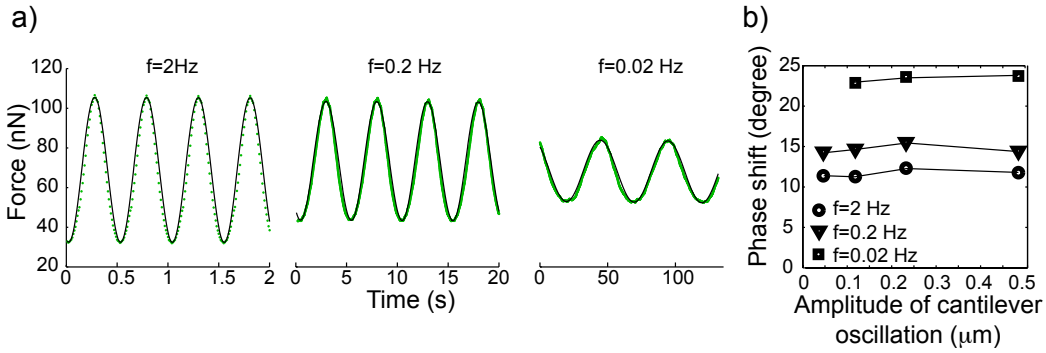

FIG. S12: Force oscillations are sinusoidal and scale linear with height amplitudes. a) Force oscillations are close to sinusoidal in shape in the measured frequency range (data: green dots, sinusoidal fit: black solid line). b) Measured phase shifts of oscillations are largely independent of the imposed oscillation amplitude of cell height up to height amplitudes of 0.5 μm . In Fig. 4c, main text, we show in addition that force amplitudes scale linearly with cell height amplitudes.

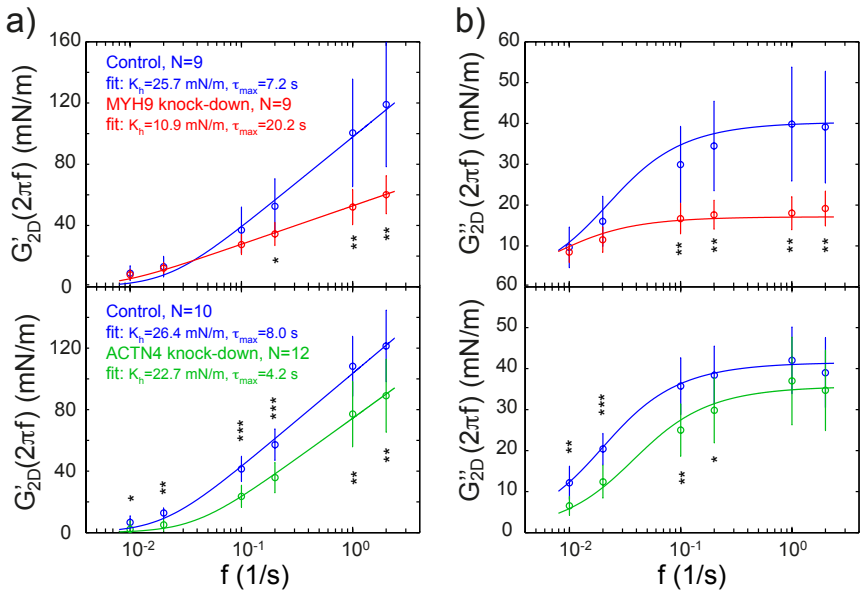

FIG. S13: Actin cross-linkers influence cortical rheology. Two-dimensional complex elastic moduli obtained from oscillatory sampling of cells after knock-down of myosin II and α-actinin-4 through RNA interference. Average storage modulus (a) and loss modulus (b) of control cells (blue) versus myosin II knock-down cells (red, top row) or α-actinin-4 knock-down cells (green, bottom row). Error bars indicate standard deviations. Associated fits of elastic moduli resultant from a constant, cut-off relaxation spectrum are indicated by solid lines. Statistical significance was determined using the Mann-Whitney-test; *, $p \leq 0.05$, **, $p \leq 0.01$, ***, $p \leq 0.001$.

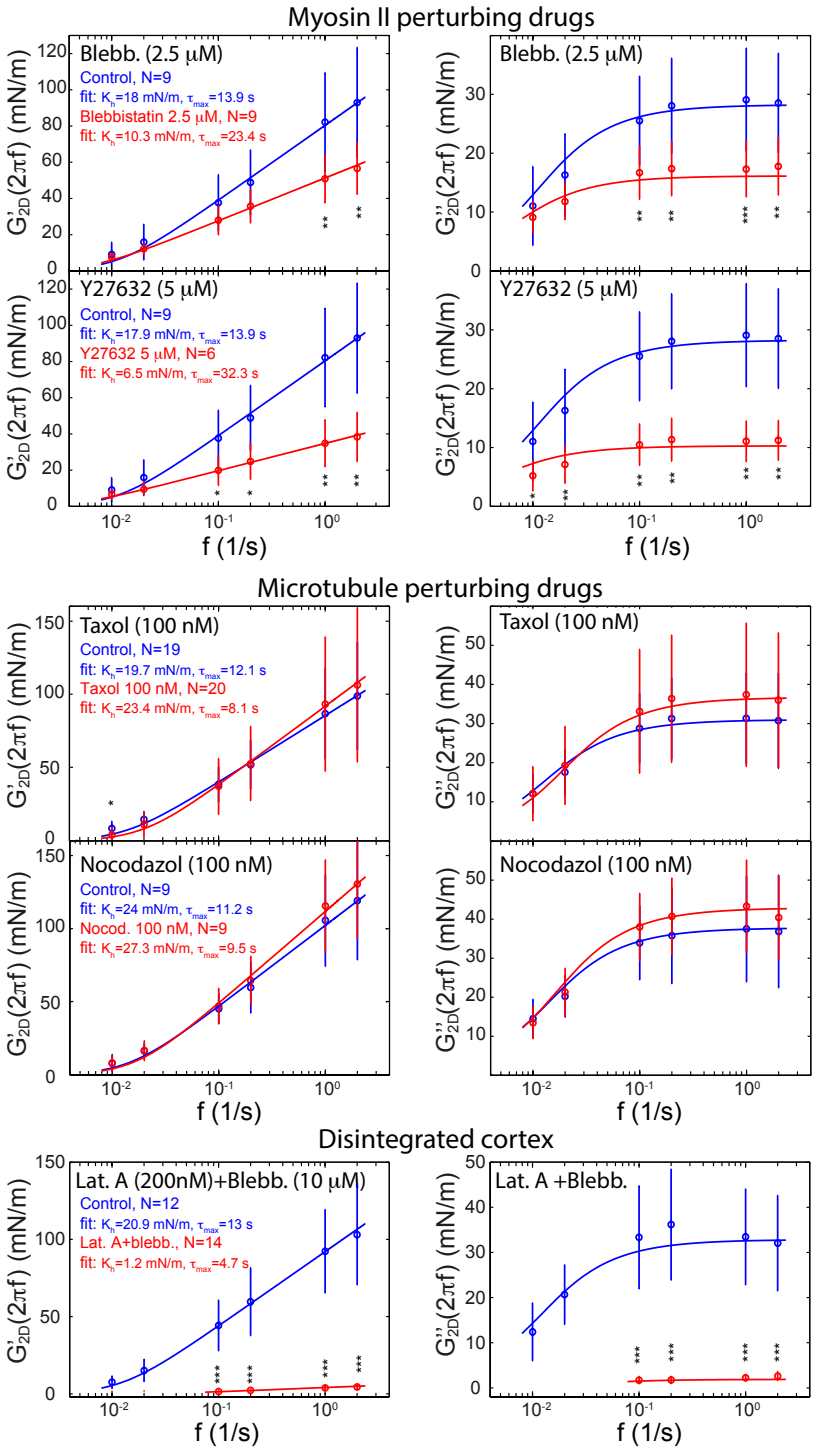

FIG. S14: Effect of cytoskeletal drugs on cortical rheology. Two-dimensional complex elastic modulus extracted from oscillatory sampling of cells after addition of cytoskeletal drugs as indicated (Materials and Methods). Average storage modulus (left) and loss modulus (right) of control cells (blue) versus drug-treated cells (red). Error bars indicate standard deviations. Fits of elastic moduli resultant from a constant, cut-off relaxation spectrum are indicated by solid lines. Statistical significance was determined using the Mann-Whitney-test; *, $p \leq 0.05$, **, $p \leq 0.01$, ***, $p \leq 0.001$. (Lat. A, latrunculin A, blebb., blebbistatin)

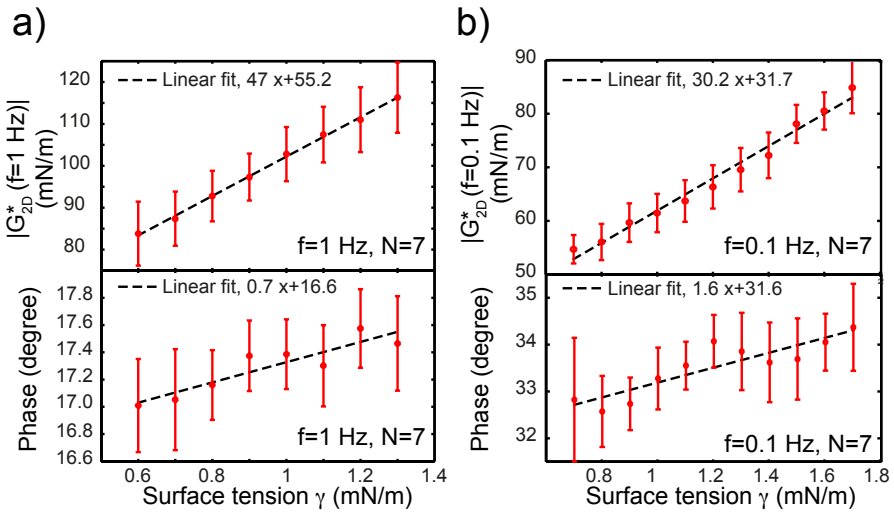

FIG. S15: Magnitude and phase of complex elastic modulus in dependence of changing surface tension as extracted from photo-inactivation experiments (Fig. 6, main text). Cells in mitotic arrest were treated with blebbistatin ($2.5-5\,\mu$M) and sampled via oscillatory cantilever height modulations. Upon exposure to blue light for $\approx$ 10s, average force and force amplitude increase. Due to active blebbistatin slowly reentering the cell, average force and oscillation amplitude gradually decrease down to their original values over a time period of $\approx$ 10min. In this time period, cell stiffness in dependence of varying cell surface tension was extracted. a,b) Averaged magnitude of elastic modulus (top row) and phase shift φ (bottom row) in dependence of estimated cell surface tension as derived from average force values for oscillation frequencies 1 Hz (a) and 0.1 Hz (b). Error bars show standard errors of the mean.

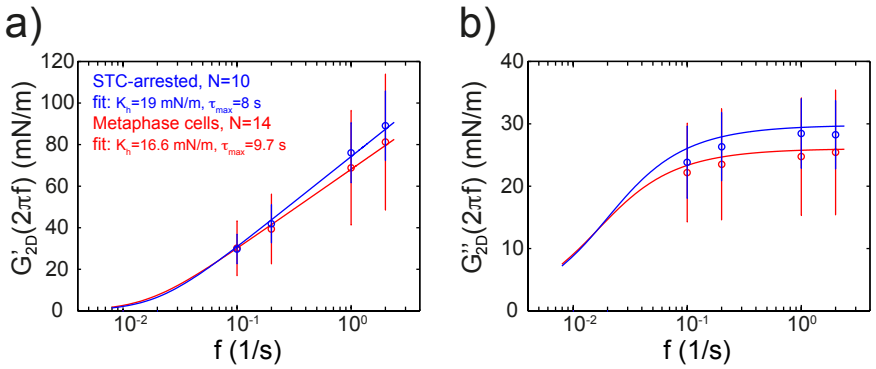

FIG. S16: Effect of mitotic arrest on cortical rheology. a,b) Two-dimensional complex elastic modulus extracted from oscillatory sampling of cells in mitotic arrest (2 μM S-Trityl-L-cysteine) or of cells in metaphase. Average storage modulus (left) and loss modulus (right) of arrested cells (blue) versus metaphase cells (red). Error bars indicate standard deviations. Fits of elastic moduli resultant from a constant, cut-off relaxation spectrum are indicated by solid lines. Cells in mitotic arrest on average show a slightly increased rheological parameter K_h ($\approx$ 14% higher, p-value: 0.04) while differences in the time scale τ_{max} are not statistically significant. Cells in mitotic arrest and in metaphase were measured at an average normalized cell height reduction of $\xi = 0.42$, both. We measured in a frequency range of $0.1 - 2$ Hz, as metaphase cells typically progressed to anaphase after ≈ 10 min and measurements of longer oscillation periods were thus not possible.

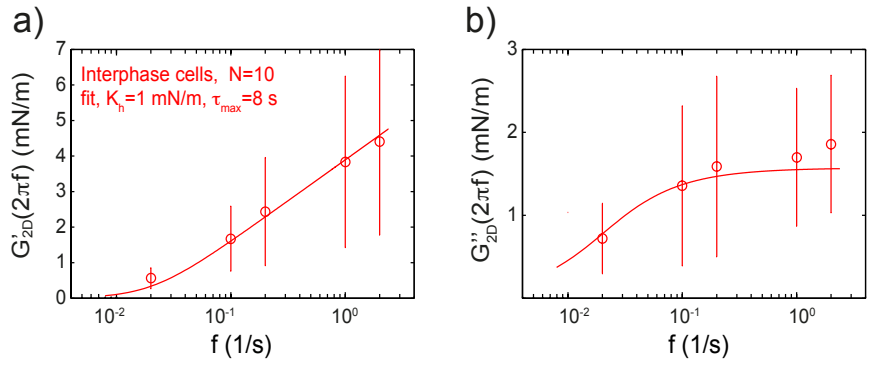

FIG. S17: Cell rheology in interphase. a,b) Two-dimensional complex elastic modulus extracted from oscillatory sampling of rounded interphase cells. Average storage modulus (left) and loss modulus (right) of interphase cells. Error bars indicate standard deviations. Fits of elastic moduli resultant from a constant, cut-off relaxation spectrum are indicated by solid lines. Cells were first detached from cell culture dishes with Trypsin/EDTA and measured on dishes coated with PLL-g-PEG (SuSoS) which prevents cell adhesion. Cells were measured at an average normalized cell height reduction of $\xi = 0.5$.